Vehling, F., Hasenclever, J., Rüpke, L. (2022):
New insights from thermohaline multiphase simulations into the mechanisms controlling vent fluid salinity following a diking event at fast-spreading ridges
Earth Planet. Sci. Lett. **597** , art. 117802

New insights from thermohaline multiphase simulations into the mechanisms controlling vent fluid salinity following a diking event at fast-spreading ridges

F. Vehling[1, 2,3], J. Hasenclever[4], L. Rüpke[1]

[1]: GEOMAR Helmholtz Centre for Ocean Research Kiel, Germany
[2]: Institute of Geoscience, Kiel University, Germany
[3]: now at Department of Environmental Informatics, Helmholtz Centre for Environmental Research - UFZ, Leipzig, Germany
[4]: Institute of Geophysics, Center for Earth System Research and Sustainability, CEN, Hamburg University, Germany

Corresponding author: Falko Vehling, GEOMAR, Helmholtz Centre for Ocean Research, Wischhofstraße 1-3 24148 Kiel | Germany
Email: fvehling@geomar.de
ORCID: 0000-0001-5712-3560

Keywords: (5)

- Mid-ocean ridges
- Magmatic diking event
- Numerical multiphase model
- Salt water phase separation
- Hydrothermal vent salinity evolution

Abstract

Hydrothermal fluids expelled at mid-ocean ridge vent sites show a large spatial and temporal variability in exit temperatures and chlorinities. At the East Pacific Rise (EPR), 9°50.3'N, time series data for a 25+ year period reveal a correlation between these variations and magmatic diking events. Heat input from dikes appears to cause phase separation within the rising fluids splitting them into low-salinity vapor and high-salinity brine phases. The intrusion of a new dike is therefore likely to result in a characteristic salinity signal, with early post-eruptive fluids showing vapor-influenced low salinity and later brine-influenced fluids showing high salinity values.

We here use a 2-D multiphase hydrothermal flow model to relate these observations to processes and properties within the sub-seafloor such as permeability, porosity, background flow rates, and phase separation as well as segregation phenomena. We have grouped the time evolution of vent fluid salinity into four temporal stages and have identified how multiphase flow phenomena control vertical salt mass fluxes within each stage. Rock porosity and permeability as well as background temperature of the undisturbed hydrothermal system control the duration of the four stages and maximum venting salinity. Based on our results, we are able to reproduce the characteristics of time-series data from the EPR at 9°50.3'N and infer the likely ranges of rock properties and the hydrothermal conditions within the oceanic crust beneath.

1 Introduction

Submarine hydrothermal systems sustain unique ecosystems, affect global-scale biogeochemical cycles, and mobilize metals from the oceanic crust to form volcanogenic massive sulfide deposits. Quantifying these processes requires linking seafloor observations to physico-chemical processes at depth. Hydrothermal flow observations at mid ocean spreading centers show a high spatial and temporal variability in vent fluid temperature, chlorinity and chemistry (Butterfield and Massoth, 1994; Gallant and Von Damm, 2006; German and Von Damm, 2004; Seyfried et al., 2011; Von Damm, 2004).

Especially at fast-spreading and intermediate-spreading ridges, where magmatic events happen several times within one century, these variations occur on relatively short time scales. At the fast-spreading East Pacific Rise (EPR) at 9°N, a focus site of international hydrothermal research, variations in vent fluid salinity and temperature have been especially well documented (Detrick et al., 1987; Fornari et al., 1998; Fornari et al., 2012). Another well-studied site is the intermediate-spreading Juan de Fuca ridge, where multiple segments of variable magmatic activity have been repeatedly surveyed contributing to an improved understanding of the hydrothermal response to eruptive diking events (Butterfield et al., 1997; Delaney et al., 1998; Wheat et al., 2020).

Here we focus on the P and Bio9 hydrothermal vents at EPR 9°50.3'N for which, a complete record of fluid temperature and chemistry exists for the time span 1991 to 2008 (Fig. 1). In late 1989, the high-temperature hydrothermal field was visually discovered in the axial summit trough including massive sulfide deposits and vent biota, but no exact temperature was measured (Haymon et al., 1991). The eruptive diking event of early 1991 had buried some of the old vent chimneys and two new chimneys (P and Bio9) started to build up near to the eruptive fissure with a distance of 50 m between them (Haymon et al., 1993). The area was further characterized by widespread diffusive venting of gray to black smoke and cloudy water from holes, cracks and pits in very glassy, new-looking lava flows and rubble. After a second eruption in late 1991 to early 1992 (Rubin et al., 1994), which did not destroy the new vents, the chlorinity of Bio9 and P vent decreased to minimum and temperature increased to maximum values (Fornari et al., 1998). Samples from the next dives showed a reduced vent temperature and rising chlorinity, which goes along with cooling and thermal cracking of the dike at greater depth inferred from recorded micro seismicity (Sohn et al., 1998; Sohn et al., 1999). After a peak in 1995/1996, chlorinity dropped again and temperature slowly rose. With the 2005/06 extrusive eruption (Tolstoy et al., 2006; Xu et al., 2014), a new cycle began with very low chlorinity and temperatures reaching their highest values. Again, this was followed by an increase of chlorinity and decrease of temperatures very similar compared to the 1991/1992 diking event (Fornari et al., 2012).

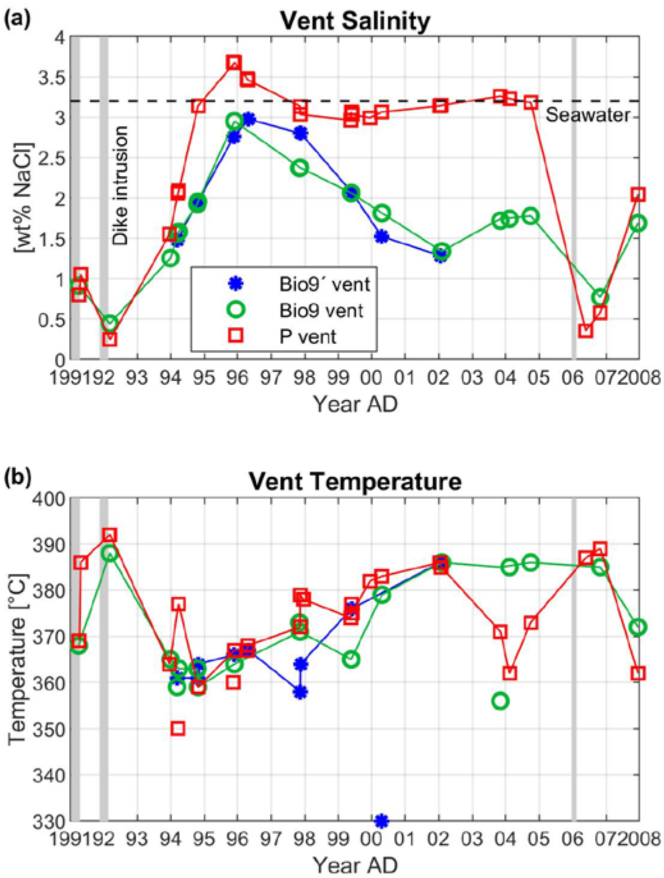

Figure 1 Salinity and temperature evolution for the Bio9, Bio9’ and P vents at EPR 9°50.3’N. Data are from Von Damm (2004) and Fornari et al. (2012). Vertical grey lines mark periods dike intrusions and associated eruptions as dated by Rubin et al. (1994) and Tolstoy et al. (2006). Thickness of lines indicates uncertainty of eruption date.

These time series observations point to a characteristic evolution of vent fluid temperature and salinity during the first few years following a diking event. The salinity of vent fluids can change, when the magmatic heat causes the rising hydrothermal fluids to separate into a high-salinity brine and a low-salinity vapor phase with differing mobilities so that the formed phases segregate (Von Damm, 1990). The buoyant vapor phase rises, condenses, and vents as a low-salinity fluid. Later the complementary denser brine phase is entrained and transported to the seafloor leading to higher salinity venting at decreasing temperatures before the vent returns to its background state, which is likely controlled by long-term phase separation phenomena on top of the axial magma lens (Vehling et al., 2021).

Such regular measurements over several years, and without major gaps, make this data set ideal for numerical investigations aimed at linking seafloor observations to processes at depth. Previous models have focused on explaining time lags and magnitudes of temperature changes following tectono-magmatic events. These models mainly used single-pass flow loop approximations and successfully explained temperature evolution curves at the East Pacific Rise at 9°N and the Endeavor Field on the Juan de Fuca Ridge by perturbations to the shallow thermal and permeability structures (Germanovich et al., 2001; Germanovich et al., 2011; Ramondenc et al., 2008; Singh and Lowell, 2015). An alternative view was presented by Wilcock (2004) who explored how processes close to the melt lens could affect vent temperature on short time scales using dynamic pressure and thermal disequilibrium models.

These previous models did not consider variations in vent fluid salinity, although the salt signal may be the more sensitive proxy to sub-seafloor processes as it travels with the pore velocity and is not, unlike the temperature signal, buffered by the rock matrix. However, investigating the salinity signal requires multiphase transport models and an equation-of-state for the system H_2O-NaCl that covers the relevant p-T-X range. One early attempt was made by Lowell and Xu (2000) who modelled two-phase seawater convection near a dike intrusion at the EPR at 9°N. The complex dynamics of multi-phase flow of saline fluid above a heat source and the vent fluid evolution in response to basal heat input variations have been investigated by several studies (Choi and Lowell, 2015; Coumou et al., 2009; Vehling et al., 2021). Yet, to our knowledge, no previous study has related the complete characteristic salinity signal following a dike event (Fig. 1) to multiphase phenomena in the sub-seafloor.

In our study we present results of several 2D multiphase simulations of a dike intrusion into a hydrothermal system at pressure conditions found at EPR 9°50.3'N (25 MPa). First, we analyze the fluid-dynamics for a reference case. This includes early phase separation phenomena like two-phase flow, brine accumulation and halite precipitation near the dike and subsequently brine mobilization and halite dissolution. In the second part we investigate the role of key parameters controlling the vent salinity evolution like rock permeability and porosity as well as the background fluid temperature and salinity within the hydrothermal upflow zone. Afterwards, we compare the simulated salinity and temperature curves to the time series data available for the P and Bio9 vents.

Table 1. Variables

variable	meaning	Value (fixed)	unit
bc	Subscript for boundary condition		-
c_d	Specific heat (dike)		J/(kg·K)
c_r	Specific rock heat	1100	J/(kg·K)

c_l	Additional specific heat between solidus and liquidus temperature (dike)	1675	J/(kg·K)
do	Subscript for downstream node		-
D	Salt diffusivity	10^{-9}	m^2/s
E	Total energy in fluid and matrix		J
E_d	Total energy of dike section		J
f	Subscript for fluid (vapor or liquid)		-
$\vec{\mathbf{g}}$	Gravitational acceleration	9.81	m/s^2
h	Subscript for halite		
h	Specific enthalpy of fluid mixture		J/kg
h_f	Fluid specific enthalpy		J/kg
h_h	Specific enthalpy of halite		J/kg
K	Mean conductivity of rock and fluid	2.5	W/(m·K)
k	Isotropic rock permeability		m^2
k_{du}	Permeability at T_{du}	10^{-17}	m^2
$k_{r,f}$	Relative permeability		-
k_{seg}	Computed permeability at segment		m^2
L	Latent heat		J
l	Subscript for liquid		-
$Q_{E,d}$	Heat flow rate of dike section		J/s
Q_m	Mass flow rate		kg/s
Q_E	Heat flow rate		J/s
Q_X	Salt mass flow rate		kg/s
$q_{E,d}$	Conductive heat flux at the dike		$J/(m^2 \cdot s)$
q_m	Mass flux		$kg/(m^2 \cdot s)$
q_X	Salt mass flux		$kg/(m^2 \cdot s)$
p	Pore pressure		Pa
p_{crit}	Pressure at critical point of H_2O	$22.06 \cdot 10^6$	Pa
p_{top}	Top pressure boundary condition	$25 \cdot 10^6$	Pa
S_h	Volumetric halite saturation		-
S_l	Volumetric liquid saturation		-
S_v	Volumetric vapor saturation		-
S_{lr}	Residual liquid saturation		-

t	Time		s
T	Rock and fluid temperature		°C
T_b	Temperature at left boundary node		°C
T_{br}	Temperature (brittle boundary)	600	°C
T_d	Dike section temperature		°C
T_{du}	Temperature (ductile boundary)	800	°C
T_l	Liquidus temperature	1200	°C
T_s	Solidus temperature	1000	°C
T_{top}	Top inflow temperature boundary condition	10	°C
up	Subscript for upstream node		-
v	Subscript for vapor		-
$\vec{\mathbf{v}}_f$	Darcy velocity		m/s
X	Mean salinity of the phases present in the pore space		wt. fraction
X_f	Fluid salt content		wt. fraction
X_{out}	Mean salt content of venting fluids		wt. fraction
w	Half-thickness of dike	1	m
η_f	Fluid viscosity		Pa·s
ρ_f	Fluid density		kg/m³
ρ	Density of fluid mixture		kg/m³
ρ_d	Dike density	2900	kg/m³
ρ_r	Rock density	2900	kg/m³
Φ	Rock porosity		-
Φ_{du}	Porosity at T_{du}	0.001	-

2 Numerical approach

2.1 Model assumptions and governing equations

We use the same numerical simulator as presented in Vehling et al. (2021), where we have demonstrated its ability to simulate the evolution of saline submarine hydrothermal systems. Here we only present the main model assumptions and governing equations. The key model features and assumptions are:

1. rock and fluid are in local thermal equilibrium
2. rock enthalpy is related to temperature by a constant specific heat
3. porosity closes at the brittle-ductile transition between 600°C and 800°C
4. relative permeability of co-existing liquid and vapor phases changes linearly with their saturation, and the liquid phase is immobile below a residual saturation
5. pressure-volume work and viscous dissipation are accounted for
6. capillary pressure effects are negligible
7. kinetic energy terms are orders of magnitude smaller than others and hence can be neglected

We solve for the conservation of fluid mass (Eq. 1) and energy (Eq. 2) and salt mass (Eq. 3):

(1) $$\frac{\partial(\Phi\rho)}{\partial t} = -\nabla\cdot\left(\sum_{\mathrm{f}\in\{\mathrm{l,v}\}}\rho_{\mathrm{f}}\vec{\mathbf{v}}_{\mathrm{f}}\right)$$

(2) $$\begin{aligned}\frac{\partial E}{\partial t} &= \frac{\partial}{\partial t}(\Phi\rho h) + \rho_{\mathrm{r}}c_{\mathrm{r}}\frac{\partial(T(1-\Phi))}{\partial t}\\ &= \nabla\cdot K\nabla T - \nabla\cdot\left(\sum_{\mathrm{f}\in\{\mathrm{l,v}\}}h_{\mathrm{f}}\rho_{\mathrm{f}}\vec{\mathbf{v}}_{\mathrm{f}}\right) + \sum_{\mathrm{f}\in\{\mathrm{l,v}\}}\frac{\eta_{\mathrm{f}}}{kk_{\mathrm{r,f}}}\vec{\mathbf{v}}_{\mathrm{f}}^{2} + \frac{\partial(p\Phi)}{\partial t} + \sum_{\mathrm{f}\in\{\mathrm{l,v}\}}\vec{\mathbf{v}}_{\mathrm{f}}\nabla p\end{aligned}$$

(3) $$\frac{\partial(\Phi\rho X)}{\partial t} = \nabla\cdot\left(-\sum_{\mathrm{f}\in\{\mathrm{l,v}\}}\rho_{\mathrm{f}}X_{\mathrm{f}}\vec{\mathbf{v}}_{\mathrm{f}}\right) + \nabla\cdot\left(\sum_{\mathrm{f}\in\{\mathrm{l,v}\}}D\rho_{\mathrm{f}}\nabla X_{\mathrm{f}}\right)$$

All variables are summarized in Table 1. Subscripts l, v, h stand for liquid, vapor and halite phase and f is either liquid or vapor. The fluid velocity through a porous medium is described by Darcy's law. Halite is treated as immobile phase and is absent in advection terms. The third term on the right-hand side of Eq. (2) describes viscous dissipation, and the fourth and fifth terms contain the part of the pressure-volume work that is not accounted for in the specific enthalpy.

(4) $$\vec{\mathbf{v}}_{\mathrm{f}} = -k\frac{k_{\mathrm{r,f}}}{\eta_{\mathrm{f}}}\left(\nabla p - \rho_{\mathrm{f}}\vec{\mathbf{g}}\right)$$

In this manuscript, the term phase saturation is defined and used as a volumetric phase saturation. Therefore, all three phase saturations sum up to one:

(5) $S_{\mathrm{l}} + S_{\mathrm{v}} + S_{\mathrm{h}} = 1$

For the calculation of the relative permeability of liquid and vapor, $k_{r,l}$ and $k_{r,v}$, respectively, we implemented a function in which the relative permeability is not additionally reduced by halite precipitation, because this is already accounted for in rock permeability in Eq. (A.8). Therefore, relative liquid permeability is a linear function from 0 to 1, when $S_l/(1-S_h)$ exceeds the residual liquid saturation S_{lr}:

(6) $$k_{r,l} = \frac{S_l/(1-S_h)-S_{lr}}{1-S_{lr}} \quad \forall S_l/(1-S_h) > S_{lr}$$
$$k_{r,l} = 0 \quad \forall S_l/(1-S_h) \leq S_{lr}$$

(7) $$k_{r,v} = S_v/(1-S_h)$$

The mean fluid density ρ, mean specific enthalpy h and mean salinity X are defined as follows, using $X_h = 1$:

(8) $$\rho = S_l\rho_l + S_v\rho_v + S_h\rho_h$$

(9) $$h = \frac{S_l\rho_l h_l + S_v\rho_v h_v + S_h\rho_h h_h}{\rho}$$

(10) $$X = \frac{S_l\rho_l X_l + S_v\rho_v X_v + S_h\rho_h}{\rho}$$

The simulator uses a Newton-Raphson approach, where a linear set of equations is solved simultaneously for the primary variables pore pressure p, specific enthalpy of fluid mixture h and salt mass fraction of fluid mixture X. These three variables uniquely describe the fluid state of the system H_2O-NaCl and are used to calculate all fluid properties and phase saturations.

2.2 Equation of state in the system H_2O-NaCl

The simulator uses the equation of state in the system H_2O-NaCl published by (Driesner and Heinrich, 2007) and Driesner (2007). Since they have not published a parameterization of fluid viscosity, we use the one by Klyukin et al. (2017). A phase diagram of the system H_2O-NaCl can be found in the supplementary material (Fig. S.1). Throughout this paper, we use the critical curve to distinguish between vapor- and liquid-like in the single-phase region at pressures higher than p_{crit} (22.06 MPa) with vapor always having a lower density than a fluid on the critical curve for a given pressure. Therefore, a “vapor” is a fluid, which has a density below the density at the critical point of pure water (321.9 kg/m³), or a fluid having a higher temperature and a lower salt content than the critical curve at a given pressure.

2.3 Model Setup

We explore dike events in a simplified setup that mimics the situation on the fast-spreading EPR. Our model domain covers one half of a two-dimensional cross section and the left boundary is the ridge axis, where dike events are simulated as dynamic boundary conditions (Fig. 2a, b). The model domain is 1 km high and 1.5 km long and we establish a hydrothermal circulation cell via a Neumann boundary condition at the bottom. At the bottom left side from 0 m to 50 m, we set a positive mass flux condition (into the domain), which is balanced by a negative mass flux boundary condition between 70 m and 1500 m so that the total bottom mass rate Q_m of inflow and outflow cancel each other out. On top of the domain, we set a pressure boundary condition (25 MPa) allowing for free venting. We further assume a uniform rock density of ρ_r = 2900 kg/m³, a rock specific heat capacity of c_r = 1100 J/(kg·K) and a mean thermal conductivity of K = 2.5 W/(m·K). The salt diffusivity is $D = 10^{-9}$ m²/s.

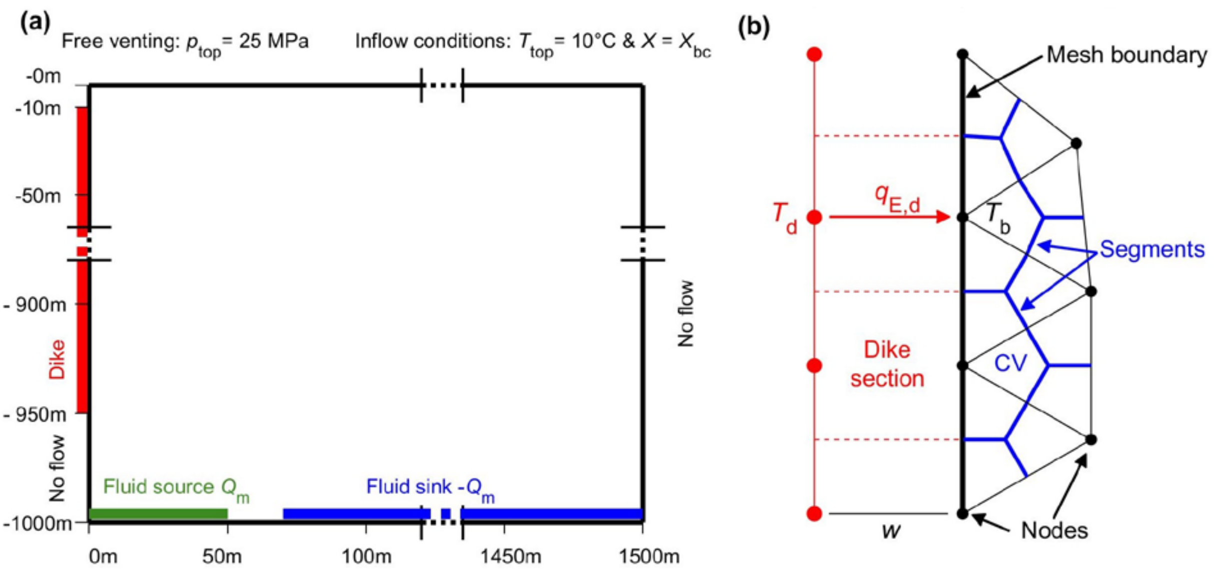

Figure 2 a Simulation domain and boundary conditions. Borders of domain are disrupted for better visualization. **b** Close up of dike boundary condition with vertical discretization of the dike in red and grid node in black.

We simulate the heat release of a cooling dike by a variable heat flux boundary condition at the left domain boundary. Note that the dike itself is not part of the modelling domain, but is virtually attached via conductive heat exchange. The dike is vertically discretized so that every boundary control volume (CV) that encloses a node has a corresponding section of the dike (Fig. 2b). The heat fluxes $q^i_{\mathrm{E,d}}$ from dike center to the domain boundary are calculated as follows for each control volume i.

(11) $$q^i_{\mathrm{E,d}} = -K\frac{\left(T^i_{\mathrm{b}} - T^i_{\mathrm{d}}\right)}{w}$$

where T_{b} and T_{d} are the temperatures of boundary nodes and dike nodes, respectively. The distance w is 1 m and is half of the total dike thickness, so that $q^i_{\mathrm{E,d}}$ represents the heat flow from the dike center to the dike edge. Converted to heat rate per CV we obtain:

(12) $$Q^i_{\mathrm{E,d}} = q^i_{\mathrm{E,d}} \cdot y^i$$

where y^i is the dike section length.

In the Appendix A we present in detail the calculation of T_{d} for each time step considering latent heat of crystalizing magma. The initial dike temperature of 1200 °C is fixed for the first four simulation days, considering that extrusive events could last for several days, during which fresh magma is flowing within the dike. Also in the Appendix A are descriptions of the implementation of relative phase permeability and for thermal closure of rock porosity for temperatures higher than 600 °C. For discretization in time, we use the theta(θ)-method with θ = 0.66 for best stability (Vehling et al. (2018). The specific phase enthalpy h_{f} and the phase salt content X_{f} are fully upwind weighted.

At a seafloor pressure of 25 MPa, a venting fluid could be in the L+V coexisting phase region, if the outflow temperature is higher than 387 °C. If this happens in the model, we calculate a mean fluid salinity X_{out} using fluid phase (salt) mass fluxes $q_{\mathrm{m,f}}$ ($q_{\mathrm{X,f}}$) out of the modelling domain at the corresponding boundary CV. The outflow flux is calculated by calculating the net mass flow rate into the boundary CV from inside the domain. This net flow rate is divided by the length of the outer border of the CV. For X_{out} the following expression holds:

(13) $$X_{\mathrm{out}} = \frac{\left(q_{\mathrm{X,l}} + q_{\mathrm{X,v}}\right)}{\left(q_{\mathrm{m,l}} + q_{\mathrm{m,v}}\right)}$$

2.4 Model simplifications

The seafloor and subseafloor structure can be amazingly complex, even at fast-spreading ridges. The employed numerical modeling framework and the presented simulation setups are not able to accurately resolve that complexity. Rather, the presented simulations have been designed to capture and elucidate first-order fluid-dynamic and thermodynamic controls on the evolution of vent fluid salinity and temperature. When interpreting the results and for relating them to observations, it is therefore important to keep some key simplifications in mind:

(1) We do not resolve the mechanics of dike emplacement and how it may alter the geometry and permeability of the hydrothermal flow zone.
(2) The sub-seafloor is approximated by a homogenous permeability that except for a reduction at the brittle-ductile transition is constant over time and not altered by the diking event.
(3) The geometry of the ridge is kept constant with time, including a constant melt lens depth.
(4) The model is two-dimensional, however, hydrothermal circulation is a self-organizing three-dimensional process, despite the 2-D characteristics of the ridge axis and the dike intrusion.
(5) We do not consider mineral precipitation reactions like anhydrite and quartz formation that can clog the pore space.

Hydrothermal circulation at fast and intermediate spreading ridges is mainly driven by the heat flow through an impermeable conductive boundary layer on top of the axial magma chamber. In our simplified model we prescribe this background state using constant inflow temperatures and salinities at the base of the 2-D model.

3 Results of a representative model run

3.1 Characteristic stages of salt transport following a dike intrusion

In this section we show detailed results for a reference simulation using the following parameters: rock permeability k = 1.5·10^{-14} m^2, rock porosity Φ = 0.05, inflow mass rate Q_{m} = 0.021 kg/s (see

Appendix A.1), residual liquid saturation S_{lr} = 0.3, bottom inflow temperature T_{bc} = 375 °C and bottom inflow salinity X_{bc} = 3.2 wt% NaCl. All time values given in figures and text are always time after the dike injection event. For the reference simulation the bottom energy input is equal to the heat release of 73 MW per 1 km ridge axis. This number agrees with the 44 MW to 71 MW per 1 km ridge axis range given by theoretical calculations of total heat flux released by crustal accretion and cooling for fast spreading ridge opening at 10 cm/yr (Fontaine et al., 2017) depending on whether lower crustal hydrothermal cooling is taken into account. The rock porosity and residual liquid saturation are in the range of other numerical simulations at fast spreading (Coumou et al., 2009; Hasenclever et al., 2014; Ingebritsen et al., 2010).

After a diking event, the evolution of vent fluid salinity can be generalized into four stages: These are the (1) venting of low-salinity liquids or vapors, (2) an increase towards elevated salinities, (3) a stage, where salinities reach a plateau around the highest values, and (4) the decrease of venting salinities to the background values before the event. Regarding the salinity curve of the Bio9 and P vent after the 1991/92 diking event (Fig. 1), stage 1 lasts until 1993/94, stage 2 until 1995 and stage 3 until 1998. Note that in stage 4 the Bio9 and P vent strongly differ in their venting salinities and local tectonic effects like flow through fractures, local brine accumulations or different background states may be responsible.

Figure 3 shows the results of an example model run to illustrate the fluid- and thermodynamic processes controlling the aforementioned stages. Plotted are the mass fluxes of the vapor and the liquid phase within 20 m distance to the dike at about 500 m below the seafloor. The left panel shows the liquid phase and the right panel shows the vapor phase at different points in time; in blank regions the corresponding phase does not exist. The intruding dike rapidly heats the fluids into the L+V coexistence region (Fig. 3a, b). Within 4 m distance to the dike, even the V+H coexisting region is reached, where halite precipitates (Fig. 3a, b). This goes along with a large volume increase of the vapor phase, which consequently expands and rises quickly due to its high buoyancy. While the upflowing and venting low-salinity vapors mark stage 1 until 1.75 years, the liquid phase remains immobile as its saturation does not yet exceed the residual liquid saturation S_{lr} limit of 0.3. During stage 1, NaCl is constantly accumulated within the expanding L+V region when rising vapors lose small amounts of NaCl. Additionally, NaCl is accumulated at the lower part of the dike at ~900m depth, where seawater recharge flow undergoing phase separation raises the NaCl content near the dike.

The second stage of rising vent salinities is initiated at 1.75 years when the liquid phase with elevated salinity starts to ascend (Fig. 3c). The cooling liquid phase exceeds its residual saturation at approximately 12 m distance to the dike and starts to rise due to its increased buoyancy. The source of this extra buoyancy is caused by a drop of density of the liquid phase, which becomes lower with decreasing temperature as the consequence of its decreasing salt content (Fig. S.2 of the supplementary material). Additionally, the above mentioned high-salinity liquids (> 20 wt% NaCl) from the lower part of the dike begin to move upwards. Stage 3 with the highest vent fluid salinities starts after 2.5 years, when due to further cooling high-salinity liquids move upwards at all distances to the dike (Fig. 3d). After 4 years most of the stored excess NaCl has been mined from the deeper parts so that liquid salinities drop below 4 wt% NaCl in the single phase region (Fig. 3e). This initiates stage 4 when vent fluid salinities return to background seawater-like values.

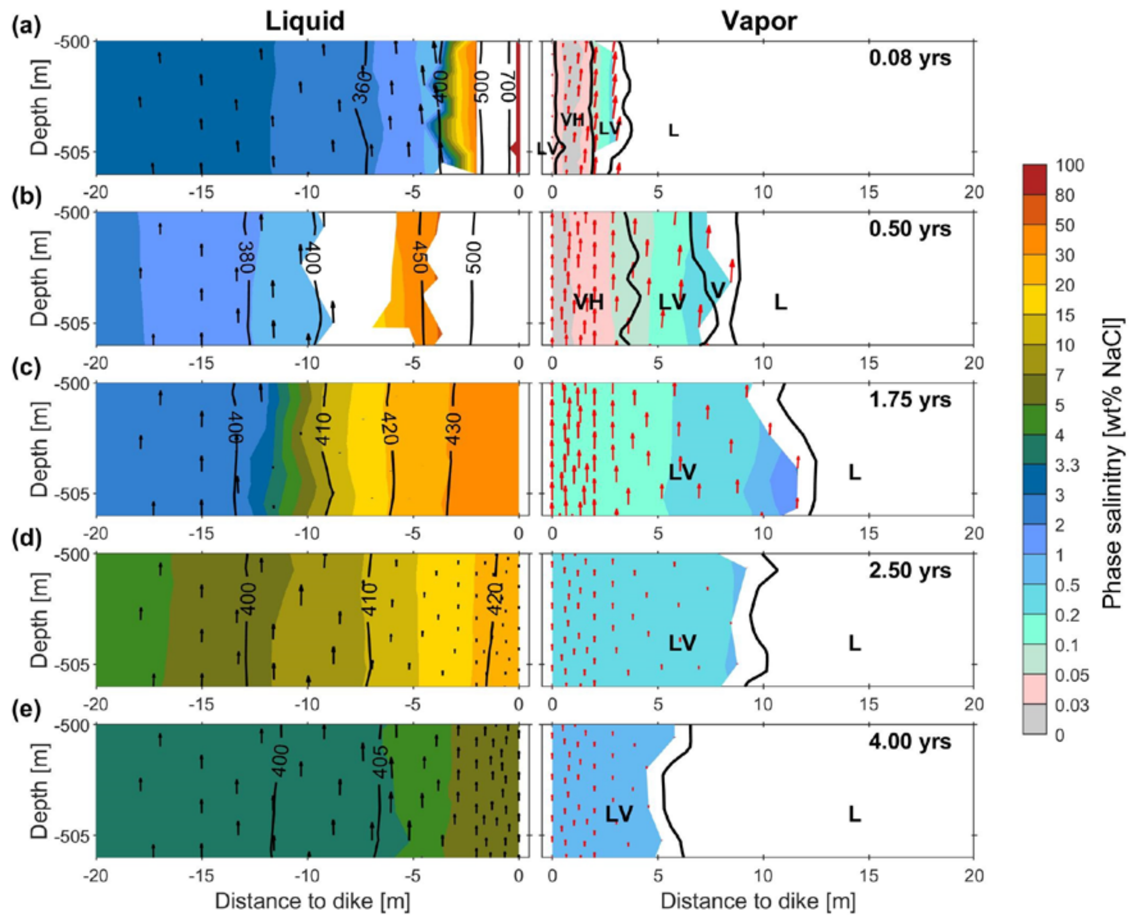

Figure 3 Results of the representative model run with parameters given in section 3.1. Contour plot of liquid (left column, mirrored) and vapor (right column) salinity at a depth of 500 m below the seafloor. The area of phase salinity color is restricted between nodes at which the same phases exist. Mass fluxes of each phase are shown as arrows with their origin at the respective grid nodes. Both

phases have the same arrow length scale of 1 m corresponding to 5.9e-4 kg/(m²·s). Black lines are isotherms in °C (left) and divide phase regions in the system H_2O-NaCl (right). This phase region boundary lines are between nodes belonging to different phase regions L: liquid, V: vapor, H: halite. LV: liquid and vapor coexistence region, VH: vapor and halite coexistence region.

3.2 NaCl accumulation and mobilization at the dike

The preceding section has shown that the saline fluids heated by the dike undergo a sequence of phase transitions. These are visualized as a temperature versus mean salinity,*X*, plot in Fig. 4 for a representative depth of 500 m below seafloor and at 2 m distance to the dike. The corresponding fluxes, the mean salinity,*X* and the porosity-dependent total salt mass per cubic meter of rock are shown in Fig. 5.

The rapid heating following a dike intrusion brings the fluids into the V+H region passing first the L+V region and then the isothermal L+V+H region (Fig. 4). Temperatures reach up to 530 °C at 2 m distance to the dike, resulting in the progressive formation and expansion of a vapor phase. This low salinity vapor phase rises buoyantly, while the increasingly saline liquid phase is still immobile as its saturation has not yet exceeded the residual liquid saturation S_{lr} limit of 0.3 (Fig. 4, Fig. 5a, b). This also results in an increase in salt mass per cubic meter rock (green lines in Fig. 5a, b), except for the about 1 m wide region next to the dike where temperatures are within the brittle-ductile transition and pore space has closed. After 0.2 years, temperatures start to fall again (Fig. 4), which causes the mean salinity to decrease because condensing vapor leads to a higher H_2O mass in pore space and a further inflow of adjacent low salinity vapor in response to the volume change. Despite the decrease in mean salinity, the salt mass per cubic meter is continuously increasing (Fig. 5a-d). The reason is that vapors continuously lose small amounts of NaCl when they are depressurized during upflow near the dike. These processes continue until 1.75 yrs, the end of stage 1 (Fig. 4 and Fig. 5c, d).

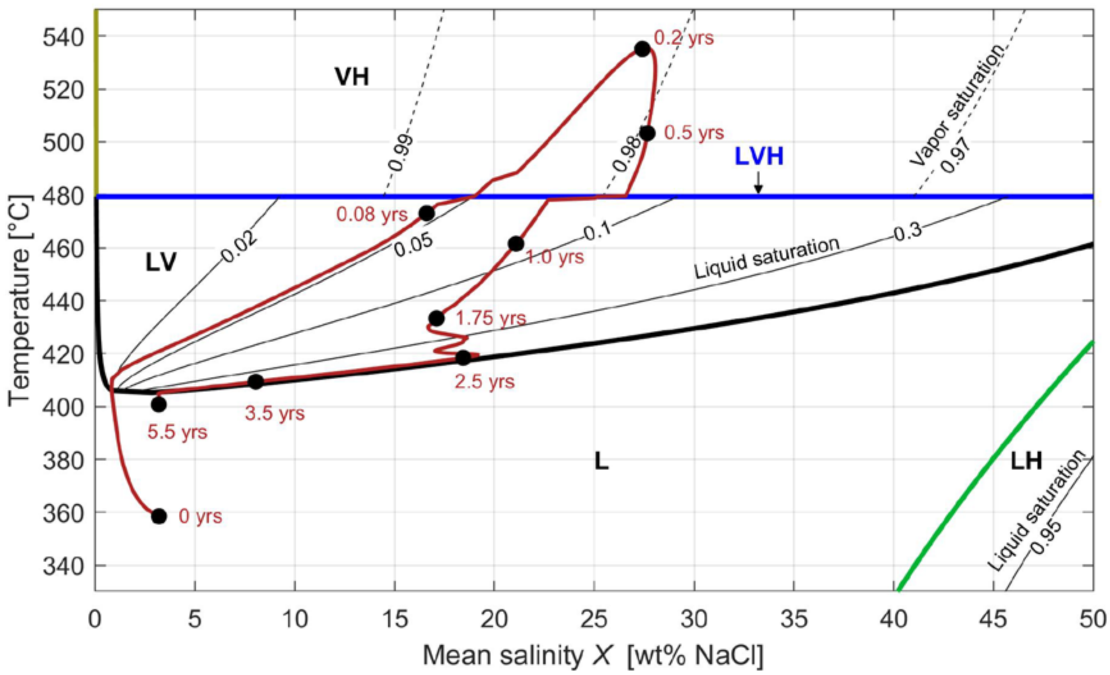

Figure 4 Temperature-salinity cross-section of the H_2O-NaCl phase diagram for a pressure of 29.4 MPa. The red line shows the temporal evolution 2 m from the dike at 500 m depth of the model calculation shown in Fig. 3. Phase boundaries shown as thick lines are the same as in the phase diagram in Fig. S.2. in the supplementary material: black: L↔LV, green: L↔LH, dark yellow: V↔VH, blue: LV↔VH. LH is liquid and halite coexistence region, LVH is the isothermal three-phase coexistence surface.

After 1.75 yrs stage 2 is initiated, when the temperature further drops within the 10 m wide L+V region, where NaCl has been accumulated (Fig. 5d). This cooling causes a strong density and salinity drop of the liquid phase (see also Fig. S.2 of the supplementary material). Simultaneously, the volumetric vapor saturation declines so that liquid saturation rises above 0.3 (Fig. 4) and the liquid phase becomes mobile. Stage 3 begins after around 2.5 years when all liquids, even those at the dike edge, have started to move upwards. This leads to the simultaneous upflow of the liquid and vapor phases within 10 m around the dike (Fig. 5e, f). The liquid phase transports the accumulated salt towards the seafloor causing the observed venting of liquids and vapors with high mean salinity. The total salt per cubic meter rock decreases accordingly between 2.5 yrs and 3.5 yrs (Fig. 5e, f). Liquid saturations remain relatively constant at 0.7 during this period and the fluid evolves along the L/L+V phase boundary (Fig. 4). After all accumulated salt has been mined, the system returns to a seawater convection without phase transitions, which is the 4th and last stage.

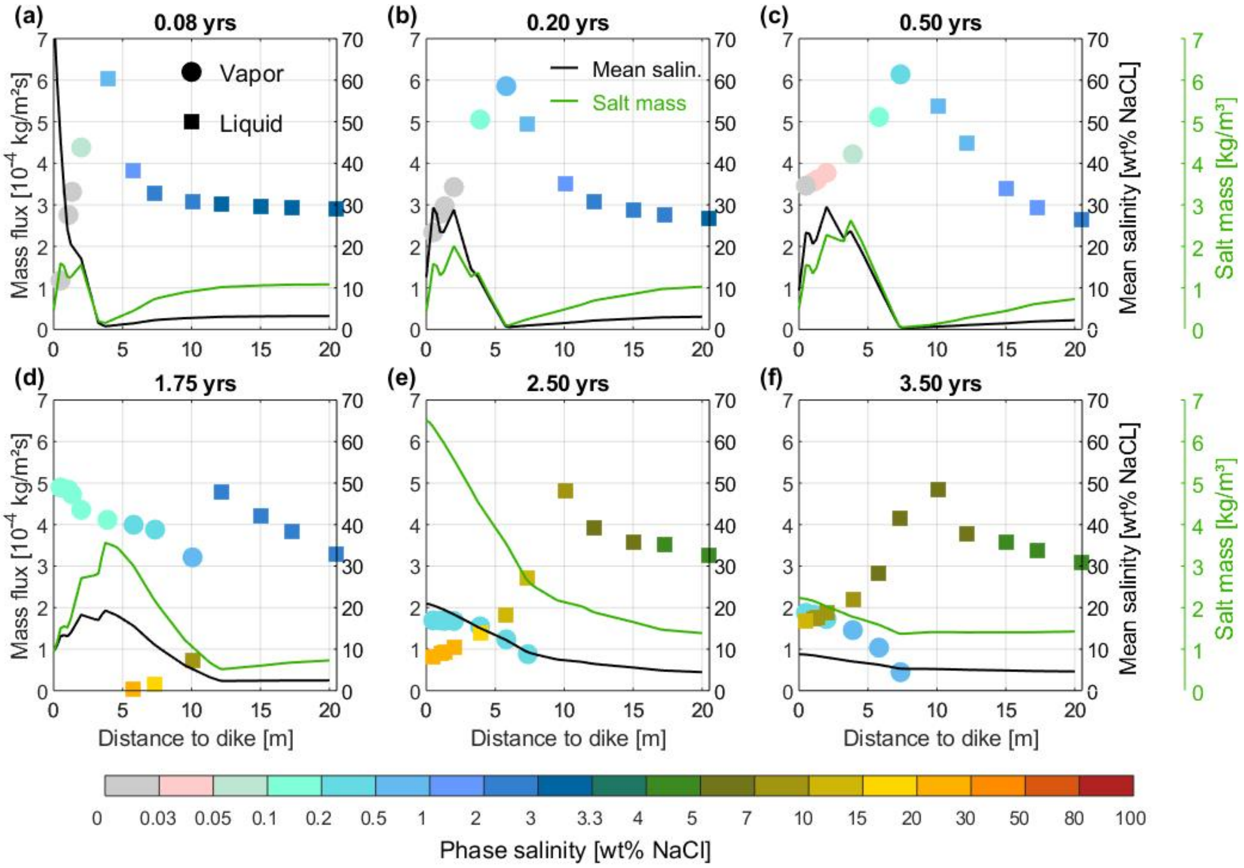

Figure 5 Mass flux analysis of the model run shown in Fig. 3. Vertical mass fluxes of vapor and liquid (circles and squares, respectively) at 500 m depth below the seafloor versus distance to the dike. Symbol color is the phase salinity. Black lines show mean salinity *X* and green lines show salt mass in pore space per cubic meter rock.

3.3 Vent salinity evolution

The vent fluid salinity evolution is directly related to the fluid- and thermodynamic processes stated above. Figure 6 shows vent fluid salinity and temperature as a function of time in the upper panel (a), discharge salt and fluid mass fluxes for the different phases in the middle panel (b), and a contour plot of the vertical mass flux as a function of depth and time in the lower panel (c). This combined figure illustrates how salt is transported from depth towards the seafloor vent site.

During the first two years (stage 1), the vent temperature is high (>390 °C) and the vent salinity is low (< 0.1 wt% NaCl). This is the consequence of very low salinity vapors rising towards the seafloor. The vapor mass fluxes (dashed red line) are relatively constant during this time (Fig. 6b). After two years (stage 2), the liquid phase saturation exceeds the residual value of 0.3 and becomes mobile. This occurs over a large depth range down to 700 m below the seafloor. Now the liquid's mass flux and salinity control the salt mass flux at the seafloor (Fig. 6b) because the vapor phase has a very low salinity in the L+V phase region. Mean salinity of the vent fluids starts to rise and exceeds the background value after approx. 2.8 yrs (stage 3). This is also a consequence of the mobilization of highly saline liquids, which have been accumulated at 700 m to 800 m depth, where phase separation of the recharge flow from below has been the source of NaCl. (Fig. 6c). The transport of NaCl at this stage can be grouped in three flow components (Fig. 5e, f). One component is the slow upward movement of high salinity liquid (>15 wt% NaCl) within the L+V region close to the dike. The second component are saline fluids that mix with the recharge flow and move upwards as a single-phase liquid with approx. 8 wt% NaCl. This upflow is strongest close to the L+V region, because here the thermodynamic relations lead to the highest buoyancy. The third component are saline liquids at some distance to the dike that are significantly diluted by recharge flow. Their discharge occurs at a distance of 15 m to 25 m with a salinity between 5 and 6 wt% NaCl. In Figure 6c, the short peak of the liquid mass flux is caused by the high sensitivity of temperature changes on the liquid density around the critical curve, shown in Fig S.2 of the supplementary material, and leads to a higher buoyancy of the single-phase liquid compared to the adjacent liquid in the hotter L+V region. At 3.5 yrs, the fluids return into the single-phase L region at 2 m distance to the dike and the observed plateau of elevated salinity venting is entirely controlled by the venting the saline liquid phase. Afterwards salinities return to the background values.

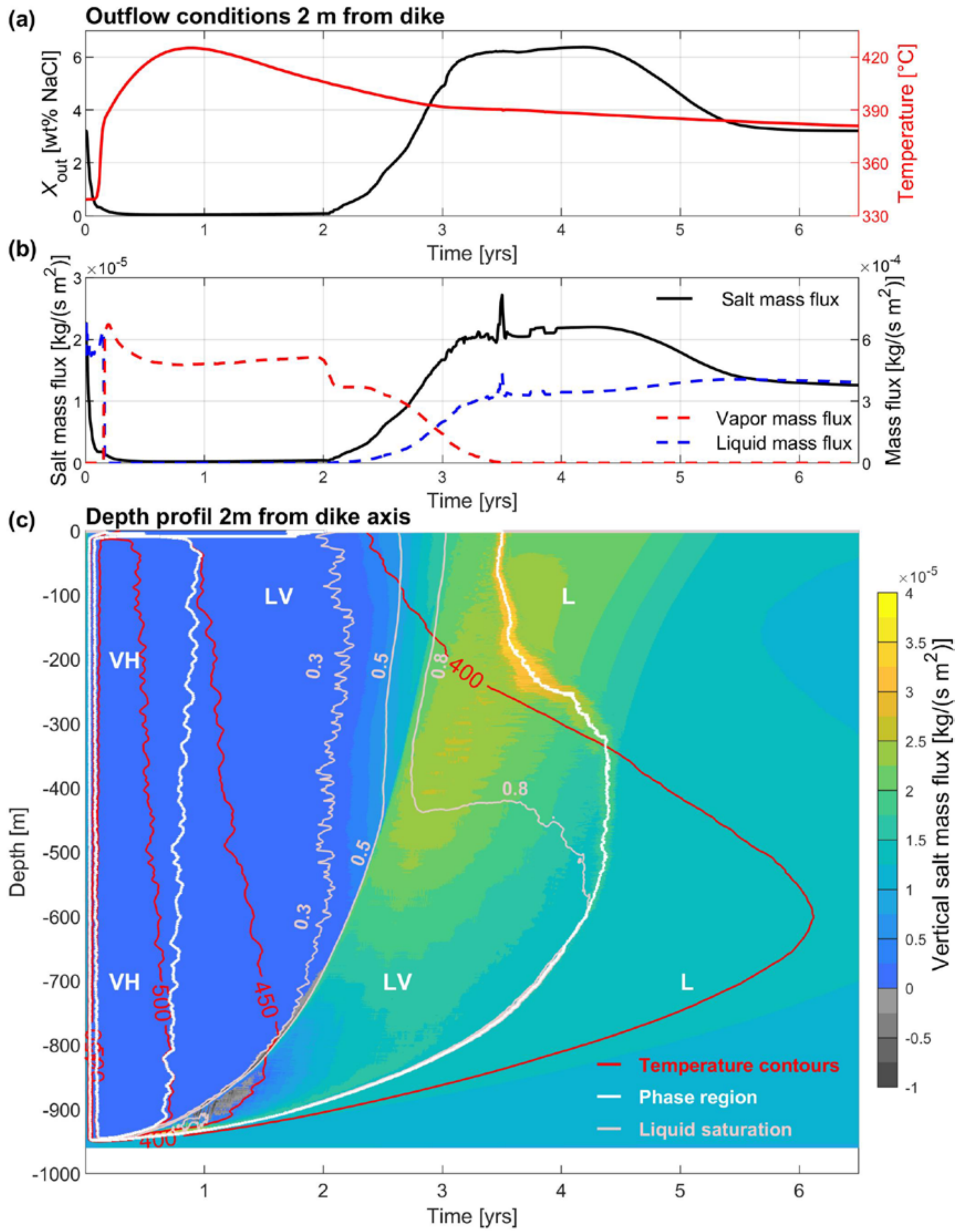

Figure 6 Temporal evolution of the representative model shown in Fig. 3. **a** Mean outflow salinity at 2 m distance to the dike versus time after the diking event. **b** Salt mass flux and mass fluxes of liquid and vapor phase. **c** Time-depth profile of vertical salt mass flux at 2 m distance to dike. Red lines are isotherms with values in °C, white lines mark phase regions, and grey thin lines mark liquid saturations.

4. Model sensitivity

While the predicted vent fluid salinity curve of the reference simulations (Fig. 6a) shows qualitative similarities to the observed variations at the EPR 9°50.3'N (Fig. 1), important differences remain. Hence, to relate observed changes in vent fluid salinity to processes at depth, an understanding is needed of how variations in model parameters affect model predictions.

4.1 Effects of inflow temperature (T_{bc}) and salinity (X_{bc})

In a first suite of sensitivity runs, we have changed the temperature and salinity of the fluids flowing from above the axial magma lens into the modeling domain. All other parameters remain the same as in the reference simulations. Figure 7a, b summarizes the results for varying inflow temperature. Panel b) shows that the temperature boundary conditions does not have a major effect on the general shape of the vent temperature curve. Variations in inflow temperature result in a linear shift of the predicted curves. The impact on the predicted vent salinity evolution curve (panel a) is, in contrast, significant. For the high-temperature case (T_{bc} = 400 °C), the time period of phase separation (stage 1) takes 1.5 years longer than in the reference resulting in dominant vapor venting until 4 years. Then a rapid change, i.e. a shortened stage 2, to a high-salinity venting occurs. The reason for the rapid onset of liquid dominated two-phase venting is a stronger pressure gradient due to the exhaustion of initially produced vapors that helps mobilize the heavier high-salinity liquids. For the lower temperature cases (T_{bc} = 325 °C and T_{bc} = 350 °C), the time duration of vapor venting (stage 1) is shortened. Most of the vapors produced at the dike condense and merge again with the high-salinity liquid phase resulting in a reduced maximum of venting salinities.

Figure 7c shows the predicted vent fluid salinity curves for different bottom inflow salinity values. Variations in X_{bc} result in a linear shift of venting liquid salinity and a small extension of stage 3 (high salinity venting) for higher values. There is no feedback on predicted vent temperatures for variations in X_{bc}.

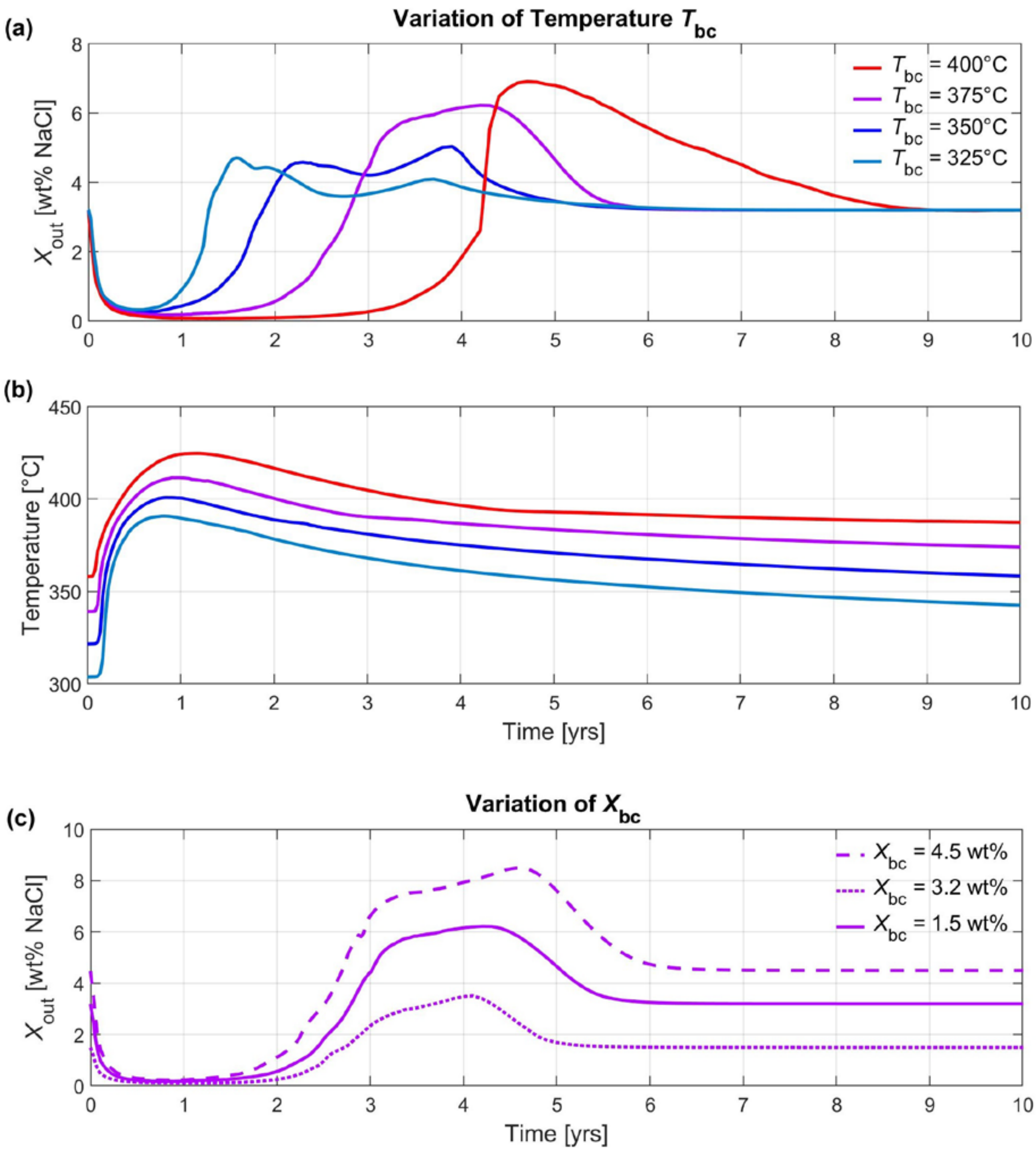

Figure 7 Model response to variations in basal temperature and salinity variations . **a** Mean outflow salinity and **b** outflow temperature for different bottom inflow temperatures T_{bc} but for same bottom inflow salinity X_{bc} = 3.2 wt% NaCl. **c** Mean outflow salinity for different bottom inflow salinities X_{bc} but for same inflow temperature T_{bc} = 375°C. Properties are averaged over a distance of 10 m from dike.

4.5 Impact of permeability and porosity

Rock permeability and porosity both affect fluid velocities and therefore have a high impact on the predicted vent fluid salinity curve. In the following suite of model runs, we use X_{bc} = 1.5 wt% NaCl and an inflow mass rate Q_m, which is linearly adjusted with rock permeability, to ensure a consistent flow field:

(14) $$Q_\mathrm{m}(k) = \frac{k}{1.5 \cdot 10^{-14}\,\mathrm{m}^2}\ 0.021\ \mathrm{kg/s}$$

Figure 8a, b shows how permeability affects vent temperature and salinity. A higher permeability leads to an earlier onset of high salinity venting (stage 3). The main reasons are a faster transport of the vapor phase and a more efficient cooling of the near dike region by enhanced fluid flow from below. The cooling causes the early condensation of residual vapor and the start of single phase liquid flow. As a consequence, stage 3 is shortened and vent fluid salinity values are predicted to return to background values more quickly. A lower permeability ($k \leq 10^{-14}\ \mathrm{m}^2$) results in a flattening of the first rise of the salinity curve because mobilized liquids of the upper part merge with low-salinity vapors from below, which ascend slower compared to the high permeability cases.

Higher permeability values are also predicted to change the venting temperature evolution. The more efficient cooling of a dike in higher permeability host rock leads to a shorter and higher temperature pulse at the vent. Note, however, that these predicted signals are also somewhat affected by the constant inflow temperature boundary condition. These prescribed inflow temperatures are independent of the fluid mass flux so that model calculations with higher permeability and hence mass flux also have a higher energy input at the base.

The impact of a lowered porosity on the predicted vent fluid salinity curve is qualitatively similar to an increase in permeability. A lower porosity, for a given permeability, results in a higher pore velocity implying a more rapid transport of the salt signal. This explains the shown salinity curves in Fig. 8c. However, the scaling for both curves is different and constant ratios between permeability and porosity can produce differing results (Fig. 8d, e). For the higher-permeability and higher-porosity case, the temperature curve (Fig. 8e) shows that vent temperatures rise earlier and to higher values compared to the lower-permeability and lower-porosity model. At the same time, the predicted vent fluid salinity evolution curves are also different for the two cases. Figure 8d shows that the higher permeability and porosity case results in a faster rise of the vent fluid salinity (stage 2).

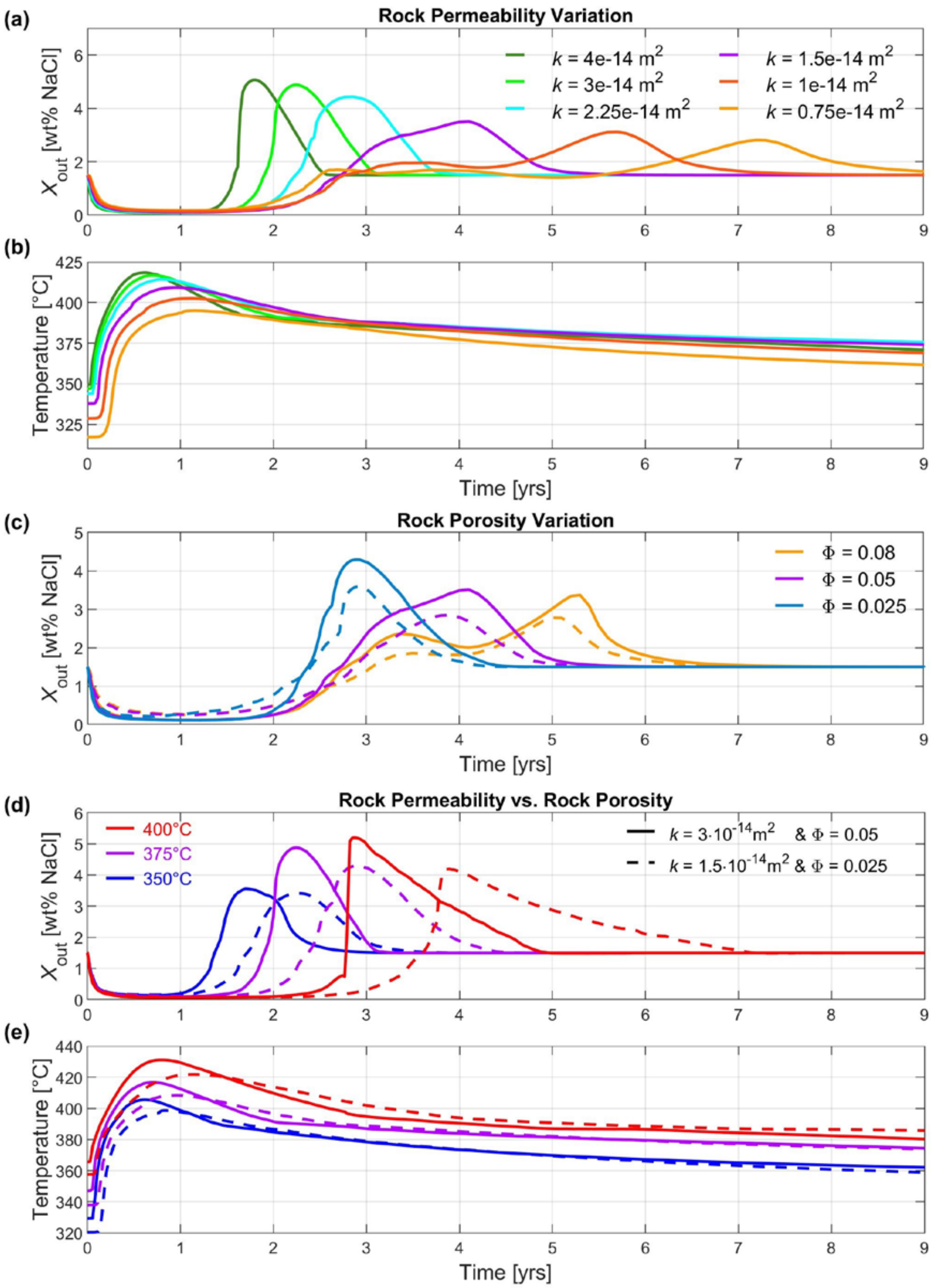

Figure 8 Model response to variations in rock porosity and/or permeability. **a** Mean outflow salinity and **b** temperature for variable rock permeability with following parameter: T_{bc} = 375 °C, Φ = 0.05, S_{lr} = 0.3. **c** Mean outflow salinity for different rock porosities with following parameters: T_{bc} = 375 °C, Φ = 0.05, S_{lr} = 0.3, $k = 1.5\cdot10^{-14}$ m^2. Continuous lines show results for residual liquid saturation of S_{lr} = 0.3 and dashed lines show results for S_{lr} = 0. **d, e** Rock permeability vs. rock porosity with S_{lr} = 0.3. Properties are averaged over a distance from 0 m to 10 m from dike.

The faster transition to higher venting salinities in the high-permeability + high-porosity model is directly linked to the earlier temperature drop towards ~400 °C. For the high-temperature simulations, cooling from below is less efficient and the maximum brine peak of both cases (stage 3) has a higher time shift. Setting the residual liquid saturation to zero has the simple effect of dampening the salinity curve (Fig. 8c) because the liquid phase can move earlier.

5 Discussion

The results have shown that we identified the key parameters controlling the salinity curve evolution after a dike intrusion. Figure 9 shows that we can approximate the salinity curve of the EPR 9°50.3'N Bio9 and P vents when we use inflow temperature and salinity of T_{bc} = 375 °C and X_{bc} = 1.5 wt% NaCl, a rock permeability of $k = 1.5 \cdot 10^{-14}$ m^2 and a rock porosity of $\Phi = 0.05$ (purple curve). Also models with slightly changed parameters such as a lower permeability (orange curve) or a higher T_{bc} combined with lowered porosity (brown curve) approximate the data reasonably well. Yet, the models tend to overpredict temperature. The observed vent temperature falls below 370 °C, which implies a higher convective cooling rate and therefore a higher permeability in the upper crustal layer. A somewhat higher permeability conforms with the 2006 diking event at EPR 9°50.3'N when temperature also dropped from 385 °C to 371 °C (Bio9 vent) and 388 °C to 361 °C (P vent) within only two years (Fornari et al., 2012). For a cooling below 380 °C, our models predicts a rapid mobilization of all produced high-salinity liquids leading to a prominent salinity peak and a fast decrease to a constant background salinity afterwards, which is not observed.

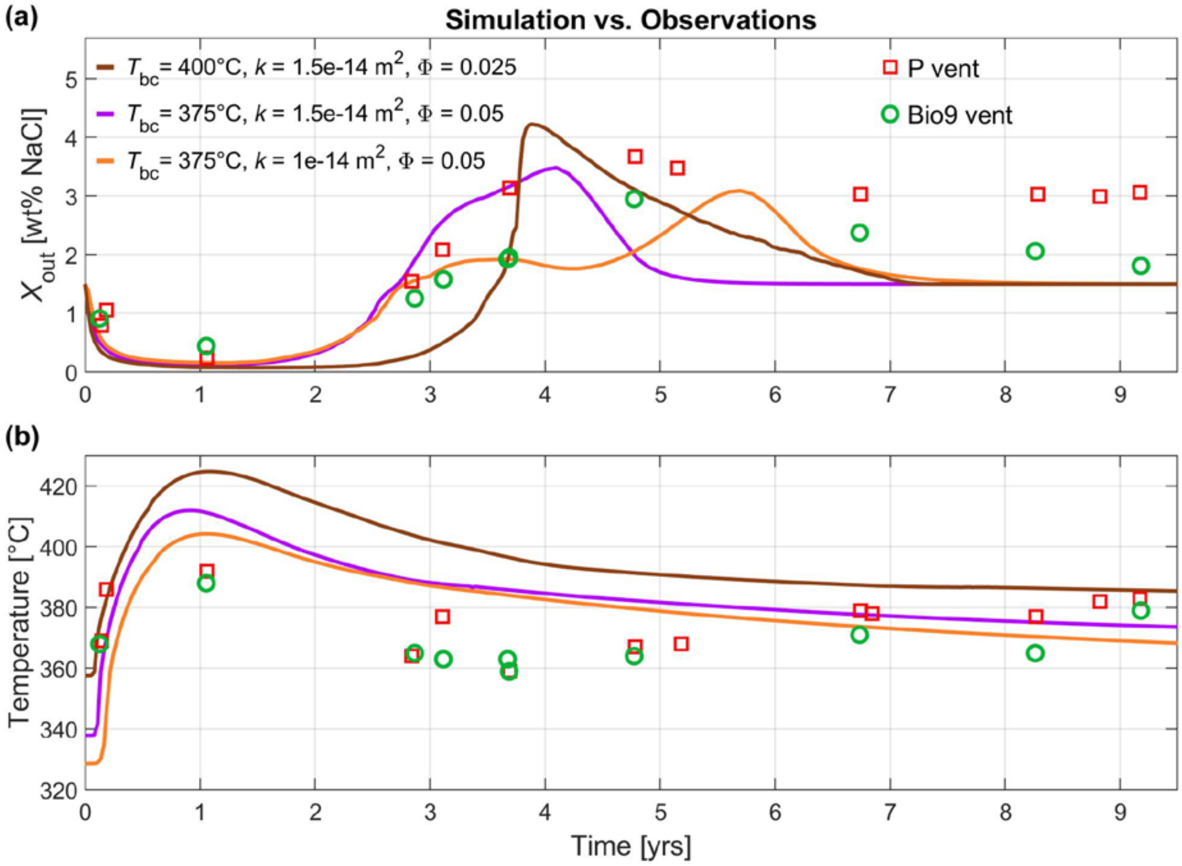

Figure 9 Best-fitting simulations for the observations at P and Bio9 vent: X_{bc} = 1.5 wt% NaCl, S_{lr} = 0.3. **a** vent salinity and **b** vent temperature. Outflow properties are averaged over a distance from 0 m to 10 m from dike.

With the help of the sensitivity analysis, we will discuss two potential reasons for these mismatches. We do not discuss further potential reasons for mismatches resulting from other model simplifications (see section 2.4) as those would not be supported by the presented results. But we would like to remind the reader of those; especially as the diking process itself is likely to impact the circulation system but that is not resolved in our modeling approach.

First, in our model, the prominent salinity peak is related to the assumption of constant rock permeability, which leads to a rather uniform cooling of the near dike region over the entire depth range and a depth-independent onset of the mobilization of high-salinity liquids (Fig. 6c). In natural systems, however, permeability is likely to change with depth (Carlson, 2011) and with distance to the ridge axis. At the axial summit trough of the EPR 9°50’N region, the thickness of the top pillow basalt layer 2A is seismically inferred to be around 155 m (Sohn et al., 2004). Borehole measurements point to an enhanced permeability on the order of 10^{-14} m^2 to 10^{-13} m^2 within an altered layer 2A (Anderson et al., 1985; Carlson, 2011). Seismic wave velocities show a significant decrease of permeability with crustal age at the ridge axis (Nedimović et al., 2008), caused by porosity decrease due to mineral precipitation. Therefore, the permeability could be higher than 10^{-13} m^2 for youngest (unaltered) created crust, where the dike intrudes, facilitating a faster advective cooling. Subsequently, the increase in vent salinity results from liquids produced and mobilized at a shallow level that merge with vapors separated at deeper parts of the dike. In addition, seawater recharge flow can be mixed into the hydrothermal upflow zone at the dike-pillow basalt transition zone. Considering that the permeability is most likely lower in the deeper parts of the sheeted dikes complex and higher in the upper parts of the sheeted dikes complex and extrusive layer 2A than our constant value, the high-salinity liquids at depth would stay in hot two-phase conditions for a longer time than predicted by our model. The dike would cool gradually with depth and the adjacent high-salinity liquids would slowly mixed into the upflow, which would lead to a more damped and smoothed salinity signal at the vent.

The second reason for dampening of the venting salinity curve could be an increasing rate of brine accumulation and upward vapor flow caused by higher heat release of a replenished and increased basal axial magma lens (AML). We think that the AML was drained after the 1991/92 event such as it had happened after the 2005/06 extrusive eruption, which resulted in extensive lava flows at the seafloor after both eruptions (Soule et al., 2009; Soule et al., 2007; Tan et al., 2016). Seismic imaging of the AML after the 2005/06 eruption also pointed to a depleted AML (Marjanović et al., 2018; Xu et al., 2014). It appears likely that the melt lens was replenished following these events with the consequence of an increased heat supply into the hydrothermal convection system leading to further phase separation phenomena. Unfortunately, the duration of AML replenishment is unknown as the observed second rise of venting temperatures after 1994 is potentially not only a consequence of the replenishment. Vent temperatures could also be affected by mineral precipitation in the uppermost layer, which can focus uprising fluids and prevent them from diffusive cooling. It is in principle possible that low-salinity vapors have mixed with high-salinity liquids at the dike and have dampened the observed salinity peak between 1995 and 1998. However, it is also likely that significant basal low-salinity vapor uprise started later and caused the salinity drop for Bio9 vent after 1997.

As Bio9 vent and P vent are direct neighbors having only a distance of 50 m between each other, it is notable that the salinity of P vent is different and stays at seawater salinity until the 2005/06 eruption. Here we think that 3D effects of fluid circulations and redistribution of upflow and downflow zones play a role after the dike has cooled. The ongoing redistribution, due to cooling, is indicated by the reduction or vanishing of venting areas observed after the dike eruption (Haymon et al., 1993; Rubin et al., 1994). The low average vent salinity of Bio9 below seawater salinity leads to a mass balance problem, which could be solved by constant NaCl accumulation on top of the AML. Numerical simulations from Vehling et al. (2021) show that stable basal brine layers are not convecting and thus strongly reduce conductive heat supply – which is needed for phase separation – from the AML into the actively convecting system. Therefore, we think that magmatic activity has significantly increased from 1995 at this ridge segment. The counterpart of this magmatic active segment is the segment 10 km to the south between EPR 9°26.1'N and EPR 9°37.1'N, where vents still have a salinity between 4.7 - 5.1 wt% NaCl during the 1991/92 eruption until 1994, where magmatic events were not observed (Oosting and Von Damm, 1996; Von Damm, 2000).

6 Conclusions

We have presented numerical simulations that relate the observed variations in vent temperature and salinity at the Bio 9 and P vents of the EPR at 9°50.3'N to subseafloor processes and properties. The employed two-dimensional models simulate the consequences of a dike intrusion into the axial part of a mid-ocean hydrothermal convection cell. The model setup considers different axial upflow temperatures and salinities using variable axial bottom boundary conditions. For a representative case study, we have analyzed how NaCl first accumulates and then is mobilized close to the dike and how this correlates to the characteristic salinity signal of seafloor vents. Within a study of parameters we found that fluid salinity and temperature of the upflow zone and the rock permeability have the highest impact on the fluid salinity curve. Rock porosity and residual liquid saturation have less significant impact.

Based on these results we were able to find the key parameters that fit the first order characteristics of the observed salinity curves at the EPR 9°50.3'N. Remaining discrepancies between model predictions and observations are related to simplifications made in the model setup with regard to homogeneous rock permeabilities and temporally constant background temperature and salinity values of the upflow zone. Our results indicate that for approximately 5 years following the 1991/92 diking event the salinity and temperature curves are strongly influenced by heat release and subsequent phase separation processes above the axial magma lens. Further simulations that combine dike intrusions with phase separation and transient brine accumulation on top of the AML should be applied to investigate how the brine layer is affected by the dike intrusion and how this is related to subsequent seafloor venting salinities.

7 Acknowledgments

Falko Vehling was funded as a doctoral candidate (scholarship) by the Helmholtz Research School Ocean System Science and Technology (HOSST). Jörg Hasenclever was funded by the German Science Foundation (DFG) through grant HA 5805-1.

8 Conflict of Interest

The authors declare that they have no conflict of interest.

9 Appendix A

A.1 Mass and heat flux boundary condition

The total mass flow rate for the bottom boundary condition was defined based on a simulation run using a Gaussian-shaped temperature boundary condition (T_{max} = 700 °C, T_{min} = 300 °C) representing the heat source of a magma chamber. We then used the total mass rate venting at the top of the domain as inflow mass rate Q_{m} and adjusted it so that a buoyancy-driven upflow of the injected fluids (350 °C to 400 °C) is established. Since we use a constant Q_{m} for all inflow temperatures, the low-temperature case of 325 °C is slightly non-buoyancy-driven. When we change rock permeability k, we change Q_{m} by the same factor.

We control the bottom inflow temperature T_{bc} by calculating the corresponding specific enthalpy h_{bc}, which also depends on inflow fluid salinity X_{bc} and bottom pressure. Therefore, h_{bc} has to be recalculated during the simulations to hold a constant T_{bc}. Total heat rate Q_{E} and salt mass flow rate Q_{X} are then defined by the following expressions:

(A.1) $Q_{\mathrm{E}} = Q_{\mathrm{m}} \cdot h_{\mathrm{bc}}$

(A.2) $Q_{\mathrm{X}} = Q_{\mathrm{m}} \cdot X_{\mathrm{bc}}$

A.2 Calculation of dike section temperatures

After each time step Δt the new dike temperatures T_{d} for each section are calculated by considering the one-dimensional (horizontal) energy conservation equation:

(A.3) $$\frac{\partial E_{\mathrm{d}}}{\partial t} = c_{\mathrm{d}} w \rho_{\mathrm{d}} \frac{\partial T}{\partial t} = -q_{\mathrm{E,d}}$$

where c_{d} is the specific heat capacity of the dike and w is the half width of the dike because we simulate one-sided cooling. The specific heat capacity c_{d} of a dike section depends on temperature because of the release of latent heat during basalt crystallization. For the interval between liquidus temperature T_{l} (1200 °C) and solidus temperature T_{s} (1000 °C), we use an additional specific heat c_{l}:

(A.4) $$c_{\mathrm{l}} = \frac{L}{\left(T_{\mathrm{l}} - T_{\mathrm{s}}\right)}$$

where $L = 3.35 \cdot 10^{-5}$ J/kg is the latent heat for basalt crystallization (Rupke and Hort, 2004)

We then define specific heat capacities for two temperature intervals:

(A.5) $$c_{\mathrm{d}} = \left(c_{\mathrm{r}} + c_{\mathrm{l}}\right) \qquad \text{if } T > T_{\mathrm{s}} \wedge T < T_{\mathrm{l}}$$

(A.6) $$c_{\mathrm{d}} = c_{\mathrm{r}} \qquad \text{if } T < T_{\mathrm{s}}$$

For calculating a new dike section temperature we then obtain the following procedure from Eq. (A.4-A.6):

(A.7) $$\begin{aligned}
T_{\mathrm{d}}^{\mathrm{new}} &= T_{\mathrm{d}}^{\mathrm{old}} - \frac{q_{\mathrm{E,d}} \Delta t}{\left(c_{\mathrm{r}} + c_{\mathrm{l}}\right) \rho_{\mathrm{r}} w} && \text{if } T_{\mathrm{d}}^{\mathrm{new}} < T_{\mathrm{l}} \wedge T_{\mathrm{d}}^{\mathrm{old}} >= T_{\mathrm{s}} \\
T_{\mathrm{d}}^{\mathrm{new}} &= T_{\mathrm{s}} - \frac{q_{\mathrm{E,d}} \Delta t - \left(c_{\mathrm{r}} + c_{\mathrm{l}}\right) \rho_{\mathrm{r}} w \left(T_{\mathrm{d}}^{\mathrm{old}} - T_{\mathrm{s}}\right)}{c_{\mathrm{r}} \rho_{\mathrm{r}} w} && \text{if } T_{\mathrm{d}}^{\mathrm{new}} > T_{\mathrm{s}} \wedge T_{\mathrm{d}}^{\mathrm{old}} < T_{\mathrm{s}} \\
T_{\mathrm{d}}^{\mathrm{new}} &= T_{\mathrm{d}}^{\mathrm{old}} - \frac{q_{\mathrm{E,d}} \Delta t}{c_{\mathrm{r}} \rho_{\mathrm{r}} w} && \text{if } T_{\mathrm{d}}^{\mathrm{old}} < T_{\mathrm{s}}
\end{aligned}$$

A.3 Permeability

When halite precipitates in regions that are strongly heated by the dike intrusion, it fills up the pore space and the rock permeability decreases. We use the following function for the reduced permeability k_i, which is also used in the TOUGH2 geothermal simulator (Pruess et al., 2012):

(A.8) $k_i = k(1-S_\mathrm{h})^2$

We computed permeability at the segments enclosing the control volumes (see Fig. 2b) using a logarithmic average, as it can vary over orders of magnitudes:

(A.9) $$k_\mathrm{seg} = \exp\left(\frac{\ln\left(k_{i,\mathrm{up}}\right)+\ln\left(k_{i,\mathrm{do}}\right)}{2}\right)$$

If halite saturation becomes larger than 0.95 at a grid point, then permeability k_seg is set to zero for all segments around this point. We then stop solving mass and salt mass conservation at these nodes, but still solve for energy conservation by heat conduction.

A.4 Thermal closure of rock porosity and reduced rock permeability

The basalts next to the dike intrusion are heated up to temperatures high enough so that they become ductile so that porosity and permeability decrease. We model a brittle-ductile transition zone for temperatures between 600 °C (T_br) and 800 °C (T_du):

(A.10) $$\Phi\left(T\right) = \frac{\left(\Phi+\Phi_\mathrm{du}\right)}{2} + \frac{\left(\Phi-\Phi_\mathrm{du}\right)}{2}\cos\left(\frac{\pi\left(T-T_\mathrm{br}\right)}{T_\mathrm{du}-T_\mathrm{br}}\right)$$

(A.11) $$k\left(T\right) = \frac{\left(k+k_\mathrm{du}\right)}{2} + \frac{\left(k-k_\mathrm{du}\right)}{2}\cos\left(\frac{\pi\left(T-T_\mathrm{br}\right)}{T_\mathrm{du}-T_\mathrm{br}}\right)$$

When the temperature exceeds 800 °C, we stop solving for mass and salt mass conservation at theses nodes, but still solve for energy conservation by heat conduction.

Appendix B. Supplementary material

The following file is the supplementary file including additional figures supporting this article.

References

Anderson, R.N., Zoback, M.D., Hickman, S.H., Newmark, R.L., 1985. Permeability versus depth in the upper oceanic crust: In situ measurements in DSDP hole 504B, eastern equatorial Pacific. Journal of Geophysical Research: Solid Earth, 90(B5): 3659-3669. https://doi.org/10.1029/JB090iB05p03659.

Butterfield, D.A. et al., 1997. Seafloor eruptions and evolution of hydrothermal fluid chemistry. Philosophical Transactions of the Royal Society of London. Series A: Mathematical, Physical and Engineering Sciences, 355(1723): 369-386. https://doi.org/10.1098/rsta.1997.0013.

Butterfield, D.A., Massoth, G.J., 1994. Geochemistry of north Cleft segment vent fluids: Temporal changes in chlorinity and their possible relation to recent volcanism. Journal of Geophysical Research: Solid Earth, 99(B3): 4951-4968. https://doi.org/10.1029/93JB02798.

Carlson, R.L., 2011. The effect of hydrothermal alteration on the seismic structure of the upper oceanic crust: Evidence from Holes 504B and 1256D. Geochemistry Geophysics Geosystems, 12(9). https://doi.org/10.1029/2011gc003624.

Choi, J., Lowell, R.P., 2015. The response of two-phase hydrothermal systems to changing magmatic heat input at mid-ocean ridges. Deep-Sea Research Part II: Topical Studies in Oceanography, 121: 17-30. https://doi.org/10.1016/j.dsr2.2015.05.005.

Coumou, D., Driesner, T., Weis, P., Heinrich, C.A., 2009. Phase separation, brine formation, and salinity variation at Black Smoker hydrothermal systems. Journal of Geophysical Research, 114. https://doi.org/10.1029/2008jb005764.

Delaney, J.R. et al., 1998. The Quantum Event of Oceanic Crustal Accretion: Impacts of Diking at Mid-Ocean Ridges. Science, 281(5374): 222-230. https://doi.org/10.1126/science.281.5374.222.

Detrick, R.S. et al., 1987. Multi-channel Seismic Imaging of a Crustal Magma Chamber Along the East Pacific Rise. Nature, 326(6108): 35-41. https://doi.org/10.1038/326035a0.

Driesner, T., 2007. The system H2O-NaCl. Part II: Correlations for molar volume, enthalpy, and isobaric heat capacity from 0 to 1000 °C, 1 to 5000 bar, and 0 to 1 X-NaCl. Geochimica Et Cosmochimica Acta, 71(20): 4902-4919. https://doi.org/10.1016/j.gca.2007.05.026.

Driesner, T., Heinrich, C.A., 2007. The system H2O-NaCl. Part I: Correlation formulae for phase relations in temperature-pressure-composition space from 0 to 1000 °C, 0 to 5000 bar, and 0 to 1 X-NaCl. Geochimica Et Cosmochimica Acta, 71(20): 4880-4901. https://doi.org/10.1016/i.gca.2006.01.033.

Fontaine, F.J., Rabinowicz, M., Cannat, M., 2017. Can high-temperature, high-heat flux hydrothermal vent fields be explained by thermal convection in the lower crust along fast-spreading Mid-Ocean Ridges? Geochemistry Geophysics Geosystems, 18(5): 1907-1925. https://doi.org/10.1002/2016gc006737.

Fornari, D.J. et al., 1998. Time-series temperature measurements at high-temperature hydrothermal vents, East Pacific Rise 9 degrees 49 '-51 ' N: evidence for monitoring a crustal cracking event. Earth and Planetary Science Letters, 160(3-4): 419-431. https://doi.org/10.1016/S0012-821x(98)00101-0.

Fornari, D.J. et al., 2012. The East Pacific Rise Between 9°N and 10°N: Twenty-Five Years of Integrated, Multidisciplinary Oceanic Spreading Center Studies. Oceanography, 25(1): 18-43. https://doi.org/10.5670/oceanog.2012.02.

Gallant, R.M., Von Damm, K.L., 2006. Geochemical controls on hydrothermal fluids from the Kairei and Edmond Vent Fields, 23°-25°S, Central Indian Ridge. Geochemistry, Geophysics, Geosystems, 7(6). https://doi.org/10.1029/2005gc001067.

German, C.R., Von Damm, K.L., 2004. Hydrothermal processes. In: Holland, H.D., Turekian, K.K., Elderfield, H. (Eds.), Treatise on geochemistry, Vol. 6. The oceans and marine geochemistry. Elsevier-Pergamon, pp. 181-222 https://eprints.soton.ac.uk/9812/.

Germanovich, L.N., Lowell, R.P., Astakhov, D.K., 2001. Temperature-dependent permeability and bifurcations in hydrothermal flow. Journal of Geophysical Research: Solid Earth, 106(B1): 473-495. https://doi.org/10.1029/2000jb900293.

Germanovich, L.N., Lowell, R.P., Ramondenc, P., 2011. Magmatic origin of hydrothermal response to earthquake swarms: Constraints from heat flow and geochemical data. Journal of Geophysical Research, 116(B5). https://doi.org/10.1029/2009jb006588.

Hasenclever, J. et al., 2014. Hybrid shallow on-axis and deep off-axis hydrothermal circulation at fast-spreading ridges. Nature, 508(7497): 508-512. https://doi.org/10.1038/nature13174.

Haymon, R.M. et al., 1991. Hydrothermal Vent Distribution Along the East Pacific Rise Crest (9°09'-54'N) and Its Relationship to Magmatic and Tectonic Processes on Fast-Spreading Midocean Ridges. Earth and Planetary Science Letters, 104(2-4): 513-534. https://doi.org/10.1016/0012-821x(91)90226-8.

Haymon, R.M. et al., 1993. Volcanic-Eruption of the Midocean Ridge Along the East Pacific Rise Crest at 9°45-52'N - Direct Submersible Observations of Sea-Floor Phenomena Associated with an Eruption Event in April, 1991. Earth and Planetary Science Letters, 119(1-2): 85-101. https://doi.org/10.1016/0012-821x(93)90008-W.

Ingebritsen, S.E., Geiger, S., Hurwitz, S., Driesner, T., 2010. Numerical simulation of magmatic hydrothermal systems. Reviews of Geophysics, 47: 33. https://doi.org/10.1029/2009rg000287.

Klyukin, Y.I., Lowell, R.P., Bodnar, R.J., 2017. A revised empirical model to calculate the dynamic viscosity of H2ONaCl fluids at elevated temperatures and pressures (≤1000 °C, ≤500 MPa, 0–100 wt % NaCl). Fluid Phase Equilibria, 433: 193-205. https://doi.org/10.1016/j.fluid.2016.11.002.

Lowell, R.P., Xu, W.Y., 2000. Sub-critical two-phase seawater convection near a dike. Earth and Planetary Science Letters, 174(3-4): 385-396. https://doi.org/10.1016/S0012-821x(99)00275-7.

Marjanović, M. et al., 2018. Crustal Magmatic System Beneath the East Pacific Rise (8°20′ to 10°10′N): Implications for Tectonomagmatic Segmentation and Crustal Melt Transport at Fast-Spreading Ridges. Geochemistry, Geophysics, Geosystems, 19(11): 4584-4611. https://doi.org/10.1029/2018GC007590.

Nedimović, M.R. et al., 2008. Upper crustal evolution across the Juan de Fuca ridge flanks. Geochemistry, Geophysics, Geosystems, 9(9). https://doi.org/10.1029/2008GC002085.

Oosting, S.E., Von Damm, K.L., 1996. Bromide/chloride fractionation in seafloor hydrothermal fluids from 9-10°N east Pacific rise. Earth and Planetary Science Letters, 144(1-2): 133-145. https://doi.org/10.1016/0012-821x(96)00149-5.

Pruess, K., Oldenburg, C., Moridis, G., 2012. TOUGH2 USER'S GUIDE, Version 2.1, Lawrence Berkeley National Laboratory, Berkeley, Calif., https://tough.lbl.gov/assets/docs/TOUGH2_V2_Users_Guide.pdf.

Ramondenc, P., Germanovich, L.N., Lowell, R.P., 2008. Modeling Hydrothermal Response to Earthquakes at Oceanic Spreading Centers. Magma to Microbe: 97-121. https://doi.org/10.1029/178GM06.

Rubin, K.H., Macdougall, J.D., Perfit, M.R., 1994. Po-210-Pb-210 Dating of Recent Volcanic-Eruptions on the Sea-Floor. Nature, 368(6474): 841-844. https://doi.org/10.1038/368841a0.

Rupke, L.H., Hort, M., 2004. The impact of side wall cooling on the thermal history of lava lakes. Journal of Volcanology and Geothermal Research, 131(1-2): 165-178. https://doi.org/10.1016/S0377-0273(03)00361-5.

Seyfried, W.E., Pester, N.J., Ding, K., Rough, M., 2011. Vent fluid chemistry of the Rainbow hydrothermal system (36°N, MAR): Phase equilibria and in situ pH controls on subseafloor alteration processes. Geochimica Et Cosmochimica Acta, 75(6): 1574-1593. https://doi.org/10.1016/j.gca.2011.01.001.

Singh, S., Lowell, R.P., 2015. Thermal response of mid-ocean ridge hydrothermal systems to perturbations. Deep Sea Research Part II: Topical Studies in Oceanography, 121: 41-52. https://doi.org/10.1016/j.dsr2.2015.05.008.

Sohn, R.A., Fornari, D.J., Von Damm, K.L., Hildebrand, J.A., Webb, S.C., 1998. Seismic and hydrothermal evidence for a cracking event on the East Pacific Rise crest at 9° 50 ' N. Nature, 396(6707): 159-161. https://doi.org/10.1038/24146.

Sohn, R.A., Hildebrand, J.A., Webb, S.C., 1999. A microearthquake survey of the high-temperature vent fields on the volcanically active East Pacific Rise (9°50′N). Journal of Geophysical Research: Solid Earth, 104(B11): 25367-25377. https://doi.org/10.1029/1999JB900263.

Sohn, R.A., Webb, S.C., Hildebrand, J.A., 2004. Fine-scale seismic structure of the shallow volcanic crust on the East Pacific Rise at 9°50′N. Journal of Geophysical Research: Solid Earth, 109(B12). https://doi.org/10.1029/2004JB003152.

Soule, S.A., Escartín, J., Fornari, D.J., 2009. A record of eruption and intrusion at a fast spreading ridge axis: Axial summit trough of the East Pacific Rise at 9–10°N. Geochemistry, Geophysics, Geosystems, 10(10). https://doi.org/10.1029/2008GC002354.

Soule, S.A., Fornari, D.J., Perfit, M.R., Rubin, K.H., 2007. New insights into mid-ocean ridge volcanic processes from the 2005-2006 eruption of the East Pacific Rise, 9°46'N-9°56'N. Geology, 35(12): 1079-1082. https://doi.org/10.1130/G23924a.1.

Tan, Y.J., Tolstoy, M., Waldhauser, F., Wilcock, W.S.D., 2016. Dynamics of a seafloor-spreading episode at the East Pacific Rise. Nature, 540(7632): 261-265. https://doi.org/10.1038/nature20116.

Tolstoy, M. et al., 2006. A sea-floor spreading event captured by seismometers. Science, 314(5807): 1920-1922. https://doi.org/10.1126/science.1133950.

Vehling, F., Hasenclever, J., Rupke, L., 2018. Implementation Strategies for Accurate and Efficient Control Volume-Based Two-Phase Hydrothermal Flow Solutions. Transport in Porous Media, 121(2): 233-261. https://doi.org/10.1007/s11242-017-0957-2.

Vehling, F., Hasenclever, J., Rupke, L., 2021. Brine Formation and Mobilization in Submarine Hydrothermal Systems: Insights from a Novel Multiphase Hydrothermal Flow Model in the System H2O-NaCl. Transport in Porous Media, 136(1): 65-102. https://doi.org/10.1007/s11242-020-01499-6.

Von Damm, K.L., 1990. Seafloor Hydrothermal Activity - Black Smoker Chemistry and Chimneys. Annual Review of Earth and Planetary Sciences, 18: 173-204. https://doi.org/10.1146/annurev.ea.18.050190.001133.

Von Damm, K.L., 2000. Chemistry of hydrothermal vent fluids from 9°–10°N, East Pacific Rise: “Time zero,” the immediate posteruptive period. Journal of Geophysical Research: Solid Earth, 105(B5): 11203-11222. https://doi.org/10.1029/1999JB900414.

Von Damm, K.L., 2004. Evolution of the Hydrothermal System at East Pacific Rise 9°50'N: Geochemical Evidence for Changes in the Upper Oceanic Crust. In: German, C.R., Lin, J., Parson, L. (Eds.), Mid-Ocean Ridges - Hydrothermal Interactions Between the Lithosphere and Oceans. American Geophysical Union, Washington, DC, pp. 285-304, https://doi.org/10.1029/148GM12.

Wheat, C.G. et al., 2020. Changing Brine Inputs Into Hydrothermal Fluids: Southern Cleft Segment, Juan de Fuca Ridge. Geochemistry Geophysics Geosystems, 21(11). https://doi.org/10.1029/2020GC009360.

Wilcock, W.S.D., 2004. Physical response of mid-ocean ridge hydrothermal systems to local earthquakes. Geochemistry, Geophysics, Geosystems, 5(11). https://doi.org/10.1029/2004gc000701.

Xu, M. et al., 2014. Variations in axial magma lens properties along the East Pacific Rise (9°30′N–10°00′N) from swath 3-D seismic imaging and 1-D waveform inversion. Journal of Geophysical Research: Solid Earth, 119(4): 2721-2744. https://doi.org/10.1002/2013JB010730.